



Non-metal doping induced dual p-n charge properties in a single ZnIn_2S_4 crystal structure provoking charge transfer behaviors and boosting photocatalytic hydrogen generation

Wei-Kean Chong^a, Boon-Junn Ng^a, Xin Ying Kong^b, Lling-Lling Tan^a, Lutfi Kurnianditia Putri^a, Siang-Piao Chai^{a,*}

^a Multidisciplinary Platform of Advanced Engineering, Chemical Engineering Discipline, School of Engineering, Monash University Malaysia, Jalan Lagoon Selatan Bandar Sunway, Selangor 47500, Malaysia

^b School of Chemistry, Chemical Engineering and Biotechnology, Nanyang Technological University, Singapore, 21 Nanyang Link, 637371, Singapore

ARTICLE INFO

Keywords:

ZnIn_2S_4
Dual p-n nature
Nitrogen doping
Photocatalytic hydrogen evolution reaction
DFT calculations

ABSTRACT

Construction of heterojunction is conventionally regarded as the prevailing technique to render effective solar-driven photocatalytic water splitting. Nonetheless, realization of p-n homojunction emerges to be an appealing scheme attributed to the non-defective layer coupling and minor charge transfer impedance. Herein, nitrogen-doped ZnIn_2S_4 (N-ZIS) with dual p-n charge properties was facilely synthesized via one-step *in-situ* solvothermal method. Systematic investigations unveil that the substituting phenomenon of hosting S by extrinsic N atom with dissimilar electronegativity and valence electron, which eventually ameliorates charge transfer rate and inhibits electron-hole pairs recombination. First-principle density functional theory calculations affirm the p-nature induced by N-doping imparting favorable charge redistribution in the ZIS framework and diminishing hydrogen (H_2) evolution reaction kinetic barrier at the surface-active sites. Therein, optimal N-ZIS generated $1575.71 \mu\text{mol} \cdot \text{g}^{-1}$ of H_2 under 6-hour visible-light irradiation (with an apparent quantum yield of 6.59 % at 420 nm monochromatic light irradiation), which is 6.35-fold than the pristine counterpart.

1. Introduction

Solar-driven water splitting for hydrogen (H_2) generation has been regarded as one of the promising strategies to overcome global energy shortage issue and to achieve overall carbon-neutral goal [1]. The intriguing prospects of solar water splitting technology is credited to the outstanding intrinsic properties of H_2 fuel such as its remarkable energy density and clean combustion nature, as well as the extraordinary sustainability in utilizing the largely abundant solar and water resources for green H_2 production. In the milieu of high-performing solar-driven H_2 generation, selection of photocatalysts is extremely critical to efficiently drive the desired H_2 evolution reaction (HER). To be classified as an ideal photocatalyst, it is essential to satisfy three key determining parameters namely: (i) excellent photon absorption ability and generation of adequate energy-content electron-hole pairs, (ii) effective charge separation and migration to the active sites, followed by (iii) spontaneous surface reactions at the solid-liquid interface.

Metal-based chalcogenide has been widely documented as one of the

most suitable semiconductor classes in photocatalytic applications accredited to the unique characteristics [2–6]. Hexagonal ZnIn_2S_4 (ZIS), one of the emblematic AB_2S_4 ternary metal chalcogenides, is a thermodynamically stable layered semiconductor with n-type behavior and a direct bandgap [7]. The appropriate and tunable bandgap from 2.06 to 2.85 eV give rise to ZIS being substantially photo-responsive towards visible light range of the solar spectrum [8]. Besides, the direct bandgap nature of ZIS grants the full utilization of photon absorption with minimal loss and induces rapid formation of electron-hole pairs. Moreover, the conduction band minimum (CBM) edge of ZIS is located at a more electronegative energy state than the reduction potential of H^+/H_2 (0 V vs. NHE at pH 0), thus bestowing the photogenerated electrons with strong reducing capability to adequately catalyze HER. On the other hand, reported studies claimed that the inherent sulfur (S) atoms on (110) facet of ZIS act as the reduction active sites and spontaneously drive surface reaction for the desired HER, without incorporation of any extrinsic co-catalyst [9,10]. The aforementioned advantages evidently crown ZIS as the potential photocatalyst in the application of

* Corresponding author.

E-mail address: chai.siang.piao@monash.edu (S.-P. Chai).

<https://doi.org/10.1016/j.apcatb.2023.122372>

Received 4 October 2022; Received in revised form 14 December 2022; Accepted 3 January 2023

Available online 4 January 2023

0926-3373/© 2023 The Authors. Published by Elsevier B.V. This is an open access article under the CC BY license (<http://creativecommons.org/licenses/by/4.0/>).

photocatalytic water splitting. With the intention to exploit the full potential of ZIS into practical application, the remaining key drawbacks of ZIS must be addressed through ameliorating the separation rate and migration kinetics of the photoinduced charge carriers.

Interface engineering is commonly considered to be a prominent approach to improve the charge transfer and separation. In general, amalgamation between two different photocatalysts could realize the formation of heterojunction or direct Z-scheme depending on the individual Fermi level [11,12]. The photocatalytic performance is significantly governed by the magnitude of the interfacial linkage [13]. Intimate interfacial connection permits effectual charge carrier transfer to achieve electron-hole pairs separation for enhanced photocatalytic performance, whereas loose interface deteriorates the performance due to the side-effects that arise from the interfacial defects. Concisely, a perfect hetero-interface with favorable charge separation is extremely challenging to be attained due to the deficient interlayer coupling, detrimental stacking orientation, unavoidable contamination and inexorable interface defect during the heterojunction formation [14–16]. Contrariwise, internal p-n homojunction within a single crystal structure is deemed to be more appealing owing to the sharp interface as well as continuous band bending for profitable carrier separation with lower impedance charge transfer pathway [17–19]. Additionally, p-n homojunction exhibits an internal electric field that further facilitates charge migration and hinders electron-hole pairs recombination [20]. Owing to the abovementioned exceptional characteristics, it is believed that the construction of ZIS with dual p-n charge nature could greatly augment the charge transfer properties and migration dynamics for efficacious HER.

Herein, elemental nitrogen (N) atom was introduced into ZIS structure in developing N-doped ZIS (N-ZIS) via a facile one-pot *in-situ* solvothermal synthetic route. Upon replacement of host S atom by extrinsic N, dual p-n charge properties have been realized within the framework utilizing the electron-deficient nature of N and the nitrogen-sulfur differential electronegativity. The optimal sample of N20-ZIS exhibits 6.35 times improvement in photocatalytic HER performance ($1575.71 \mu\text{mol} \cdot \text{g}^{-1}$ of H_2) under 6-hour visible light irradiation. Besides, the apparent quantum yield of N20-ZIS was measured to be 6.59 % (420 nm), which was significantly higher than the pristine counterpart (0.53 %). Experimental characterizations elucidate the promoted charge transfer and suppressed electron-hole pairs recombination contributing to the photoactivity improvement. First-principle calculations are provided to support the experimental claims and impart fundamental insights on the role of N inducing charge redistribution and elevating HER kinetics of doped ZIS.

2. Experimental section

2.1. Materials

Analytical grade reagents were used directly without purification, including zinc chloride (ZnCl_2 , $\geq 98\%$, Merck), indium (III) chloride tetrahydrate ($\text{InCl}_3 \cdot 4\text{H}_2\text{O}$, $\geq 97\%$, Sigma Aldrich), thioacetamide ($\text{C}_2\text{H}_5\text{NS}$, $\geq 99\%$, Nacalai Tesque), N,N-dimethylformamide ($\text{HCON}(\text{CH}_3)_2$, $\geq 99.8\%$, Macron) and ethanol ($\text{C}_2\text{H}_5\text{OH}$, $\geq 96\%$, Fisher Scientific). Deionized water (resistivity $\geq 18 \text{ M}\Omega \text{ cm}$) obtained from Millipore Milli-Q water purification system was used in the experiment.

2.2. Samples preparation

Pristine and N-doped ZnIn_2S_4 were synthesized via a simple one-step solvothermal method. 0.5 mmol of zinc chloride (ZnCl_2), 1.0 mmol of indium chloride tetrahydrate ($\text{InCl}_3 \cdot 4\text{H}_2\text{O}$), and 2.0 mmol of thioacetamide (TAA) were dissolved in a 30 mL aqueous solution containing x mL of N,N-dimethylformamide (DMF) and 30-x mL of deionized water (DI). The solution was stirred continuously and transferred into a Teflon-lined stainless-steel autoclave subjected to 160°C for 12 h. After cooling

to room temperature, the solid powder was subjected to thorough washing with ethanol and DI. The final product was finally obtained upon overnight drying in a vacuum oven at 40°C . Pristine ZnIn_2S_4 was produced when $x = 0$ and denoted as ZIS. Nitrogen-doped ZnIn_2S_4 was synthesized when $x = 10, 20$ and 30 , labelled as N10-ZIS, N20-ZIS and N30-ZIS, respectively.

2.3. Characterizations

Bruker D8 Discover X-ray diffractometer equipped with Ni-filtered $\text{Cu K}\alpha$ radiation was utilized to perform XRD analysis and investigate the crystallographic properties of different samples. Phoibos 100 spectrometer with monochromatic $\text{Al-K}\alpha$ X-ray source was used in obtaining XPS measurements. Following that, field emission scanning electron microscope (FESEM) – Hitachi SU8010, and high-resolution transmission electron microscope (HRTEM) – JEOL JEM-2100 F, equipped with EDX spectroscopy were used to characterize the structural, surface morphology and elemental composition of all the synthesized samples. Micromeritics 3Flex surface characterization analyzer was utilized to perform multipoint surface area analysis with nitrogen gas via static volumetric method. Cary 100 UV-Vis spectrophotometer – Agilent equipped with an integrated sphere and BaSO_4 reflectance standard, was used to obtain the UV-Vis diffused reflectance spectra. The bandgap was determined by KM function versus the energy incident light plots. Besides, fluorescent spectrometer – Perkin Elmer LS55, was used to obtain steady-state photoluminescence (PL) spectra. DeltaPro fluorescence lifetime system – Horiba Scientific, with an excitation wavelength of 317 nm was used to acquire time-resolved photoluminescence (TRPL) spectra.

2.4. Photoelectrochemical measurement

All the photoelectrochemical (PEC) measurements were conducted using Metrohm Autolab electrochemical workstation with a conventional three-electrode PEC setup in a 0.5 M Na_2SO_4 electrolyte solution ($\text{pH} = 6.84$). Pt was used as the counter electrode whereby Ag/AgCl saturated with 3.0 M KCl was utilized as the reference electrode. The sample was uniformly coated onto FTO glass substrate with a 1 cm by 1 cm active area, which acted as the working electrode. Throughout the analysis, the working electrode was illuminated by a 500 W Xe arc lamp equipped with an optical filter ($\lambda > 400 \text{ nm}$) and a fixed sample-to-lamp distance of 10 cm. For the transient photocurrent response, the working electrode was subjected to the light source at an intermittent on-off light rate of 20 s interval with an applied potential of 0.1 V. Following that, EIS measurements were conducted under a supply voltage of 100 mV across a frequency range from 10 mHz to 100 kHz. On the other hand, LSV analysis was conducted at an intermittent on-off light with 20 mV potential interval from -1.0 to 1.0 V . Lastly, Mott-Schottky plots were measured in the range of -0.6 to 1.0 V with a potential step of 0.05 V.

2.5. Photocatalytic performance evaluation

30 mg of photocatalyst was firstly dispersed homogeneously in 60 mL aqueous solution containing 0.35 M Na_2S and 0.35 M Na_2SO_3 . Subsequently, the solution was transferred into a Pyrex top-irradiated vessel with quartz window and bubbled with high flow rate of N_2 gas for half-an-hour. Following that, the reactor was irradiated using 350 W Xe arc lamp with an optical filter ($\lambda \geq 400 \text{ nm}$) for H_2 generation. The gas was directed to a gas chromatograph – Agilent 7820 A TCD Ar carrier gas, for online measurement of H_2 content. Besides, the apparent quantum yield (AQY) was evaluated under monochromatic light using 420 nm band pass filter following the equation:

$$\text{AQY}(\%) = \frac{N_c}{N_p} \times 100\% = \frac{2n_{\text{H}_2} N_A h c}{I S t \lambda} \times 100\% \quad (1)$$

where N_e is the total reactive electron, N_p is the total incident photon, n_{H_2} is the amount of H_2 molecule generated at time t (in mol), N_A is the Avogadro constant, h is the Planck constant, c is the speed of light, I is the light intensity, S is the irradiation area and λ is the wavelength of monochromatic light.

2.6. Computational details

The theoretical structures were optimized using Vienna Ab initio simulation package (VASP) with projected wave (PAW) method and reciprocal space with plane-wave basis [21]. DFT computations were implemented with generalization-gradient approximation (GGA) and exchange-correlation function of Perdew-Burke-Ernzerhof (PBE). Basic plane-wave settings include 500 eV of energy cut-off, 1×10^{-5} eV of energy convergence, 0.01 eV/Å of force convergence [10]. Hybrid functional Heyd-Scuseria-Ernzerhof (HSE06) was employed in the study. All the atoms were allowed to relax and an additional 15 Å vacuum layer was applied to eliminate any possible interaction between periodic images [22]. The Monkhorst-Pack k-point mesh was set at $3 \times 3 \times 1$. A pristine structure consisting of 2×2 at. bilayer with 56 total atoms (8 Zn atoms, 16 In atoms and 32 S atoms), was utilized in the study. Grimmer's DFT-D3 method was accounted as additional Van der Waals (vdW) correction factor in H_2 adsorption study for higher accuracy of interatomic forces, potential energy and stress tensor computation [23]. Additionally, the computed valance band VBM and CBM were evaluated according to Mulliken electronegativity theory [24]. The absolute electronegativity of the structure is evaluated as the geometric mean of the Mulliken electronegativity of the constituent atom (i.e., arithmetic mean of the atomic first ionization energy and the electro affinity) in the structure.

3. Results and discussion

3.1. Synthesis and structural characterization

The fabrication of N-ZIS via the facile one-step *in-situ* solvothermal was exemplified in Fig. 1. Typically, stoichiometric Zn:In:S precursors ratio of 1:2:4 was dispersed uniformly in a solution containing N, N-dimethylformamide (DMF) as N-dopant source. The doping concentration was controlled by adjusting the volume of DMF in the aqueous solution, which was 0, 10, 20 and 30 mL of DMF corresponding to the formation of ZIS, N10-ZIS, N20-ZIS and N30-ZIS, respectively. Throughout the solvothermal reaction, two-dimensional (2D) nanosheet was primarily formed due to the inherent bilayer crystal structure. Subsequently, the high surface-energy 2D structure would reassemble into a three-dimensional (3D) microsphere to modulate the surface energy for a thermodynamically stable structure [25]. The surface morphologies and microstructures of the synthesized samples were examined by field emission scanning electron microscope (FESEM) and high-resolution transmission electron microscope (HRTEM). FESEM

images (Figs. 2a and 2b) reveal the formation of flower-like microsphere configuration for both pristine ZIS and N-doped N20-ZIS (optimal) samples. It could be observed that N20-ZIS structure possesses higher sphericity with a greater fraction of intersecting nanoflakes. Such configuration not only benefits the exposure of active surface, but also enriches the light absorption capability resulting from the scattering and multilevel reflection of incident ray in the hierarchical microsphere structure [26]. TEM analysis as depicted in Fig. 2c further confirms the formation of hierarchical N20-ZIS microsphere convened by packing of nanoflakes. Interplanar spacing of 0.33 nm as shown in Fig. 2d resembles the representative hexagonal ZIS d_{102} spacing [27], indicating the hexagonality of the ZIS structure is preserved after the introduction of substitutional N dopant.

Energy dispersive X-ray (EDX) analysis was then conducted to disclose the atomic distributions within the structures. As presented in Fig. 2e and S1, it can be clearly observed that the elements (Zn, In and S) were evenly distributed in the pristine ZIS structure. Besides, uniformly doping of N atom was achieved in all the modified structures. Interestingly, inspection of the scan suggests an existence of correlation between N-doping concentration and the microsphere structure. Monitoring the N atomic percentage (N %), it is spotted that for N % lower than ca. 3.5 at %, the structures of N10-ZIS (underdoped) and N20-ZIS (optimal-doped) remain high sphericity. Excessive introduction of N into ZIS structures induces significant distortion giving non-spherical N30-ZIS structure (over-doped), as shown in Fig. S1. Additionally, Brunauer-Emmett-Teller (BET) analysis shown in Fig. S2 demonstrates that N-doping altered the morphology accompanied by the change of specific surface area of the structures. Specifically, N20-ZIS exhibits more than 100 % increment in specific surface area than that of pristine ZIS owing to the greater proportion of intersecting nanoflakes as illustrated from the FESEM imaging. Contrariwise, the overly doped N30-ZIS suffers from ca. 37 % reduction in specific surface area (see Fig. S2) due to overly doping induced unfavorable structural distortion as of previously mentioned. Following that, X-ray diffraction (XRD) analysis was conducted to acquire the crystallographic and phase structure. As depicted in Fig. 2f, pristine ZIS displays all the indexed characteristic peaks (JCPDS #03-065-2023) [28] with major diffraction peaks located near 27.6° and 47.2° corresponding to the (102) and (110) planes, respectively. As a consequence of introducing smaller atomic size of N to substitute relatively larger intrinsic S from the structure [29], it is not astonishing to expect a slight shifting of N-ZIS XRD patterns as compared to pristine ZIS. Focusing on the diffraction peak associated to (110) plane, positive shift of diffraction angle greater than 0.4° is observed for both N10-ZIS and N20-ZIS structures. As stated in Bragg equation that larger diffraction angle denoting smaller lattice, it is undoubtedly demonstrated that N atom has been successfully doped into the structures which induces lattice shrinkage. However, as indicated by the significant negative shift of diffraction angle of N30-ZIS as compared to both the N10-ZIS and N20-ZIS, it is undeniably asserted that N30-ZIS framework re-enlarges. In other words, overly doping of heteroatom

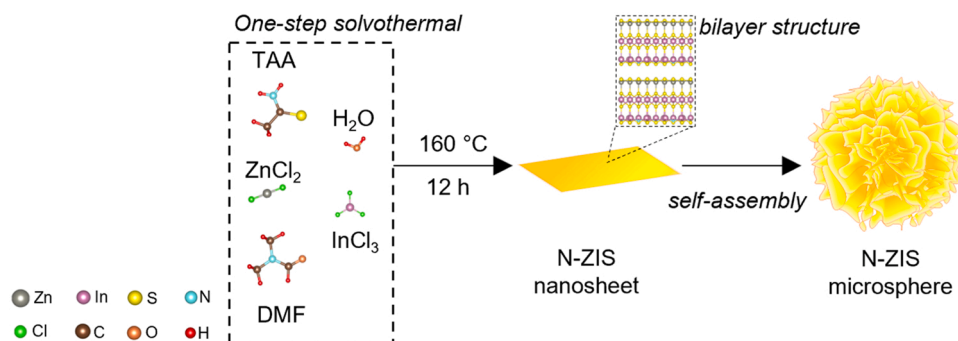


Fig. 1. Illustration of N-ZIS synthetic process via one-step solvothermal approach.

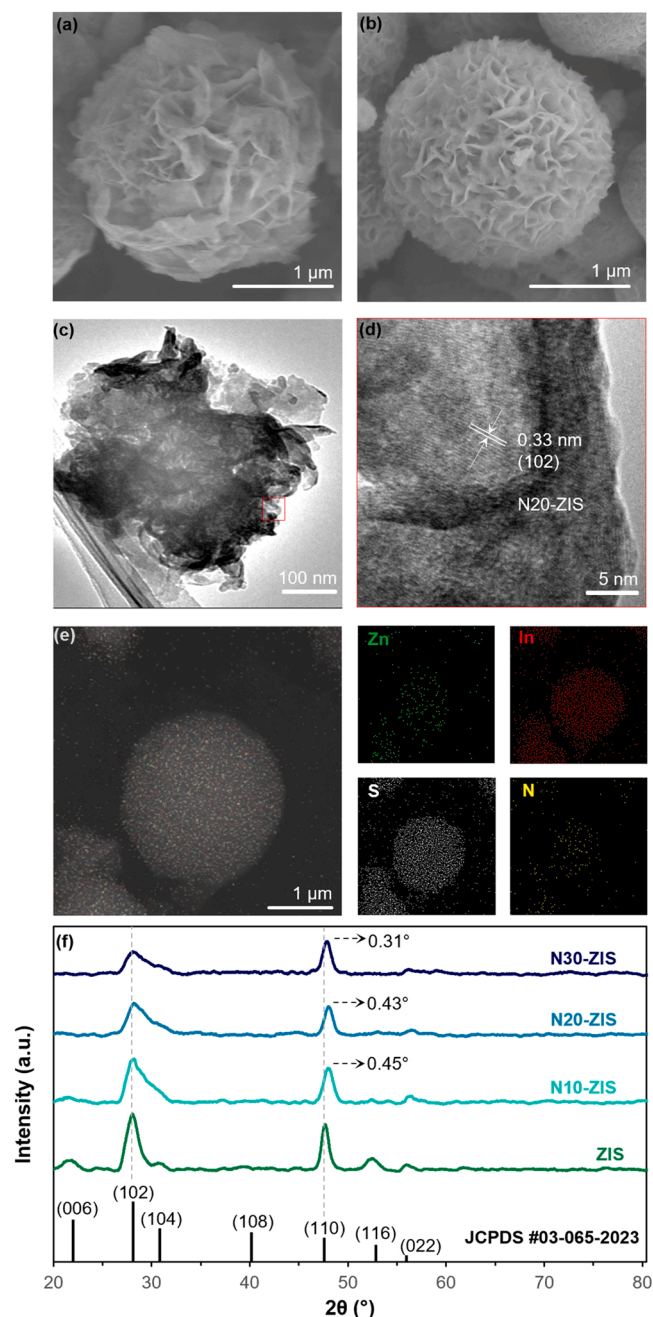


Fig. 2. FESEM images for (a) ZIS and (b) N20-ZIS. (c) TEM image of N20-ZIS and (d) HRTEM of N20-ZIS showing enlarged site-of-interest indicating lattice spacing. (e) EDX image and corresponding elemental mapping of N20-ZIS with Zn, In, S and N elements. (f) XRD spectra of the respective samples.

would eventually distort the structure, which is coherent with the FESEM findings.

X-ray photoelectron spectroscopy (XPS) was adopted to interpret the surface electronic environment of the synthesized structures, wherein pristine ZIS and optimized N20-ZIS served as representative samples for analysis. From the full XPS survey scan spectra in Fig. S3, it is evidently reflecting the presence of Zn, In and S as the major constituent elements in ZIS, with additional N peak in N20-ZIS, which implies the absence of external impurities in the synthesized samples. As shown in Figs. 3a and b, both the metallic elements are split into two corresponding peaks, namely $2p_{3/2}$ and $2p_{1/2}$ for Zn 2p peak, as well as $3d_{5/2}$ and $3d_{3/2}$ for In 3d peak. Furthermore, bi-deconvoluted peaks are observed for S 2p peaks which are contributed by the spin-orbit splitting of S $2p_{3/2}$ and S

$2p_{1/2}$ as reflected in Fig. 3c. Congruently, it is patently noticed that all the binding energies of N20-ZIS undergo slight negative translation in relation to that of ZIS. Arising from the successful replacement of host S atom by guest N atom with dissimilar electronegativity, the differential elemental electronic attraction ability induces surrounding charge redistribution, which eventually leads to binding energies (Zn, In and S) shifting [30]. Notably, only N20-ZIS structure exhibits N 1s peak (Fig. 3d), which directly confirms the existence of N in fact brought by N dopant instead of atmospheric N_2 adsorption. The splitting of N 1s peak into two dissimilar peaks around 399.4 and 401.1 eV is attributed to the existence of metal-N bonding and N species in the N20-ZIS system [31]. The findings above established successful substitution doping of N atom into the ZIS framework.

3.2. Photocatalytic H_2 evolution performance

On the account of the fact that surface proton (H^+) adsorption holds a relationship towards photocatalytic H_2 performance, zeta potential measurement was conducted to replicate the superficial electronegativity of the samples. As presented in Fig. 4a and S4, the measured zeta potential values for the individual samples are found to be -31.1 mV (ZIS), -36.9 mV (N10-ZIS), -40.2 mV (N20-ZIS) and -31.9 mV (N30-ZIS). Detailly, N20-ZIS possesses substantially more negative zeta potential followed by N10-ZIS, N30-ZIS and ZIS. In general, increment of superficial electronegativity favors the surface adsorption of positively charged H^+ for boosting of photocatalytic HER [32–34]. Thus, it is hypothesized that the efficacy of photocatalytic H_2 generation performance also follows the trend from N20-ZIS, N10-ZIS, N30-ZIS to ZIS. Noting that the difference between the samples is the presence of N, it can be securely deduced that the deviation of surface electronegativity is contributed by the N heteroatom promoting charge redistribution across the framework. Subsequently, a detailed experiment was conducted to evaluate the photocatalytic performance of the respective samples under visible light irradiation ($\lambda \geq 400$ nm). As shown in Figs. 4b and 4c, all the samples are found to be capable in driving photocatalytic HER, where the trend of photocatalytic H_2 evolution rate is in good concordance with the zeta potential. Such observation insinuates the surface charges positively impacts the H^+ adsorption for HER. In particular, the pristine ZIS exhibits poor H_2 evolution of merely $41.37 \mu\text{mol}\cdot\text{g}^{-1}\cdot\text{h}^{-1}$. Introduction of N-dopant into ZIS remarkably boosts the HER performance with N10-ZIS demonstrating $187.17 \mu\text{mol}\cdot\text{g}^{-1}\cdot\text{h}^{-1}$ of H_2 evolution. Optimal doping of 3.53 at % (N20-ZIS) demonstrated the highest H_2 yield up to $1575.71 \mu\text{mol}\cdot\text{g}^{-1}$ under six-hour continuous visible light irradiation ($262.62 \mu\text{mol}\cdot\text{g}^{-1}\cdot\text{h}^{-1}$), which is ca. 6.35 times compared to that of pristine ZIS. N20-ZIS also exhibits high stability by retaining more than 95 % performance over three repeated cyclic tests as shown in Fig. S5. The striking improvement should be attributed to the introduction of N heteroatom into ZIS framework ameliorating the charge transfer behavior and electron-hole pairs separation. Nevertheless, over doping hampers the HER performance in which tremendous reduction of H_2 yield was observed for N30-ZIS with only a rate of $87.06 \mu\text{mol}\cdot\text{g}^{-1}\cdot\text{h}^{-1}$. The finding signifies that over doping induces unfavorable lattice distortion and might create a non-desirable charge recombination center. Following that, apparent quantum yield (AQY) measurement was conducted on the pristine ZIS and the best-performing N20-ZIS samples. According to Fig. 4d, pristine ZIS shows merely 0.53 % AQY under 420 nm monochromatic light irradiation, whereas N20-ZIS displays a remarkably stable AQY of ca. 6.59 % under the same condition. The observation suggests a higher photon-to-hydrogen conversion ability of N20-ZIS that is capable in full utilization of the photoinduced charge carriers for driving the desired HER, resulting from the incorporation of N atom in the ZIS structure. Owing to different experimental conditions in determining gas evolution, AQY at specific wavelength shall be adapted for direct comparison on the efficiencies amongst photocatalysts [1,35,36]. In this work, single component N20-ZIS demonstrated relatively high AQY at monochromatic wavelength of

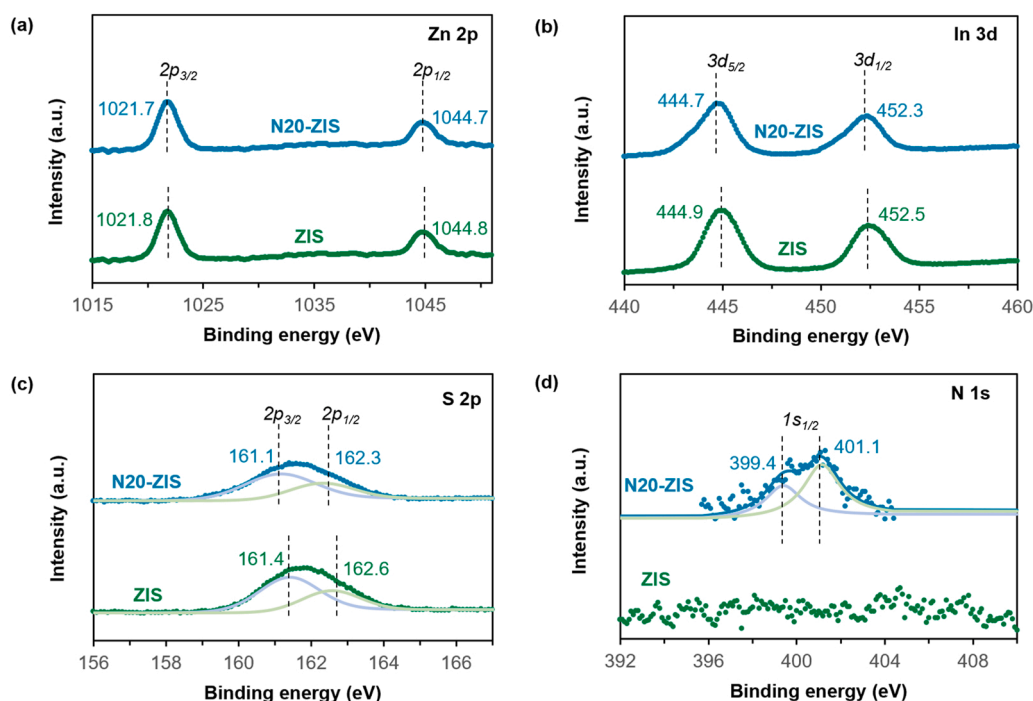


Fig. 3. XPS spectra for ZIS and N20-ZIS: (a) Zn 2p, (b) In 3d, (c) S 2p, and (d) N 1 s.

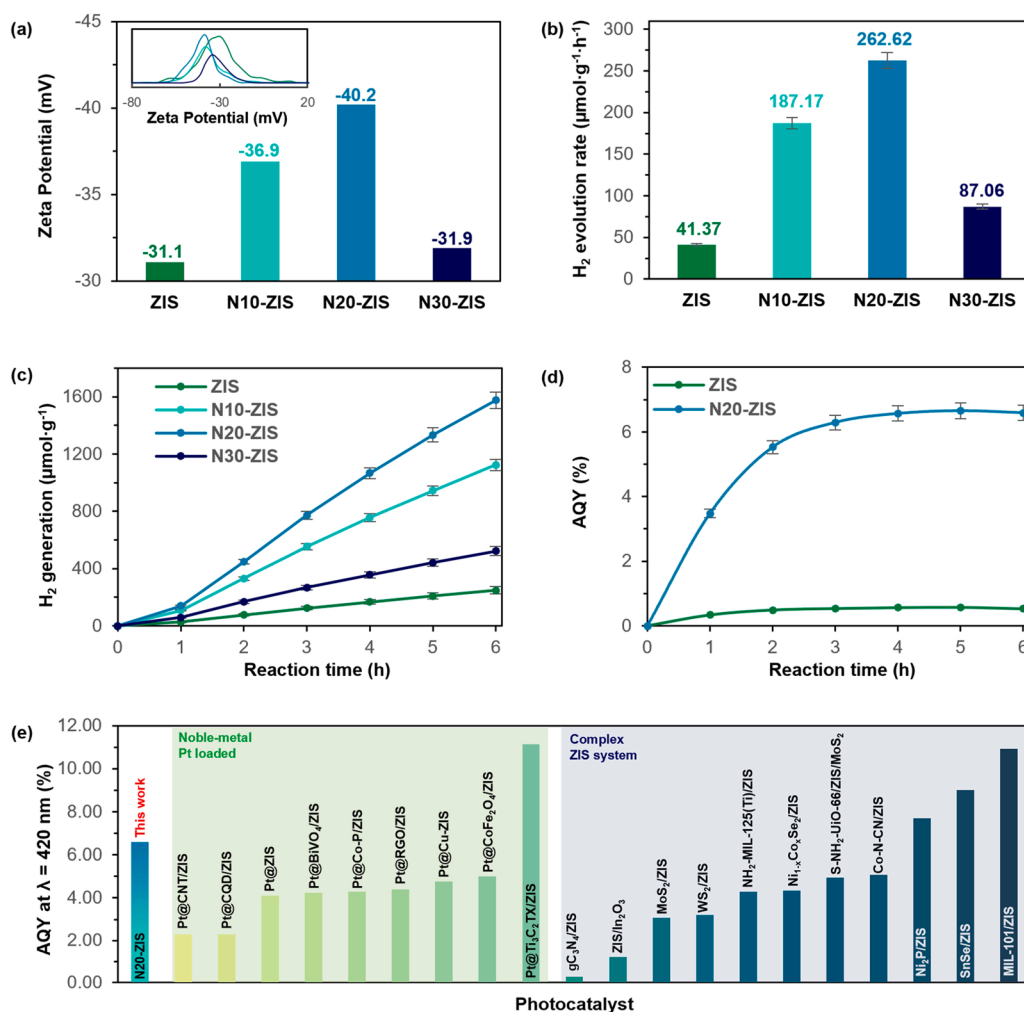


Fig. 4. (a) Zeta potential value for the respective samples (inset showing the relative frequency distribution across potentials). (b) Rate of H₂ evolution and (c) Time-dependent H₂ generation of the respective samples under visible light irradiation. (d) Measured AQY for ZIS and N20-ZIS samples under 6-hour irradiation of 420 nm monochromatic light. Dotted points dictate the arithmetic mean spanned within the maximum and minimum values, denoted by the vertical error bars. (e) Comparison between 420 nm AQY in this work with other recently reported conventional ZIS-based heterostructure.

420 nm as compared to other noble-metal loaded and complex ZIS-based heterostructure systems (see Fig. 4e and Table S1).

3.3. Photophysical and electrochemical properties

To unveil insights of the enhanced photocatalytic H_2 generation performance, various characterizations were conducted to scrutinize the underlying mechanisms. Preliminarily, the light absorption characteristic was evaluated via ultraviolet-visible (UV-Vis) diffuse reflectance spectra (Fig. 5a). It is observed that N-doped samples experience blue shifting in light absorption accompanied by the dopant-induced color change (see Fig. S1). It is worth noticing that despite pristine ZIS demonstrating the strongest light absorption capability, the pristine sample exhibits the lowest performing photocatalytic H_2 yield (refer to Fig. 4b). This observation implies that light absorption should not be considered as the predominating factor for photocatalytic activity. Optical bandgap (E_g) of the respective samples were evaluated using Kubelka-Munk (KM) equation for direct bandgap semiconductor as in Eq. (2) [37].

$$\alpha h\nu^2 = B(h\nu - E_g) \quad (2)$$

whereby α is the energy dependent absorption coefficient, h is the Planck constant, ν is the frequency of photon and B is the KM function arbitrary constant. As shown in Fig. 5b and S6, all the N-doped structures possess slightly larger E_g than pristine ZIS due to the doping-induced blue shifting of light absorption as discussed. Notwithstanding the fact that E_g of N20-ZIS (2.72 eV) is marginally greater than ZIS (2.67 eV), N20-ZIS remains visible-light active and demonstrates a remarkably better photocatalytic H_2 performance with AQY of 6.59 % at $\lambda = 420$ nm as compared to the pristine sample (0.53 % AQY). This is potentially due to the reason that light absorption capability is not the main limiting factor for photocatalytic efficacy of ZIS. Henceforth, additional aspects such as charge transfer mechanisms and interfacial reaction kinetics were taken into consideration to provide insights of the improvement.

Inspired by the capability of a single heteroatom (nitrogen family) doping propagates p-type behavior for the intrinsic n-type metal chalcogenide semiconductors [20,38–40], the potential of realizing dual p-n charge properties in ZIS via N-doping was examined. The degree of

N-doping and the respective empirical formulas of N-ZIS samples were tabulated in Table S2. It is straightforward to deduce that the minimum atomic doping percentage required is 14.3 at % to achieve a complete N-doped ZIS unit cell ($Zn_1In_2S_3N_1$), which is clearly unaccomplished in this work. Providentially, the imperfection allows the coexistence of pristine n-ZIS with elemental doped p-ZIS. For instance, arithmetical analysis infers that N20-ZIS ($ZnIn_2S_{3.75}N_{0.25}$) consists of 3:1 ratio of n-ZIS to p-ZIS, which is competent to render the configuration of dual p-n charge properties. Mott-Schottky (MS) analysis was performed to ascertain the charge conductivity nature. As illustrated in Fig. 5c and Fig. S7, pristine ZIS holds a straight positive gradient that reflects an n-type semiconductor characteristic. Conversely, N20-ZIS displays an inverted “V-shape” vortexed around 0 V, which uncover the presence of nanoscale dual p-n charge nature [41]. Linear sweep voltammetry (LSV) analysis also ascertains the presence of p-type behavior in N20-ZIS from the relatively higher cathodic photocurrent responses throughout the negative applied potential region as shown in Fig. S8, which is consistent with other reported studies [42]. The fascinating phenomenon is arisen from the defect-free substitution of S by extrinsic N (one valence electron less) atom which provides the p-type property [43]. It is worth noting that the N20-ZIS still embraces the momentous n-type semiconductor behavior (reversal to the positive slope in MS, and greater anodic photocurrent response in the LSV at higher positive voltage) owing to the dominant species being the pristine n-ZIS as deliberated. To sum up, the coexistence of p- and n-type nature in the structure synergistically endows the dual p-n charge properties in N20-ZIS framework. Notably, the MS slope of N20-ZIS is situated well below pristine ZIS across the diverse potential regions. This indicates a higher charge carrier density of N20-ZIS according to the inverse-proportionality relationship between gradient and charge density [44]. Precisely, the acceptor (N_a for p-type) and donor (N_d for n-type) densities were computed following Eqs. (3) and (4) [45].

$$N_a = -\frac{2}{qe\epsilon_0} \cdot \frac{1}{\text{gradient}} \quad (3)$$

$$N_d = \frac{2}{qe\epsilon_0} \cdot \frac{1}{\text{gradient}} \quad (4)$$

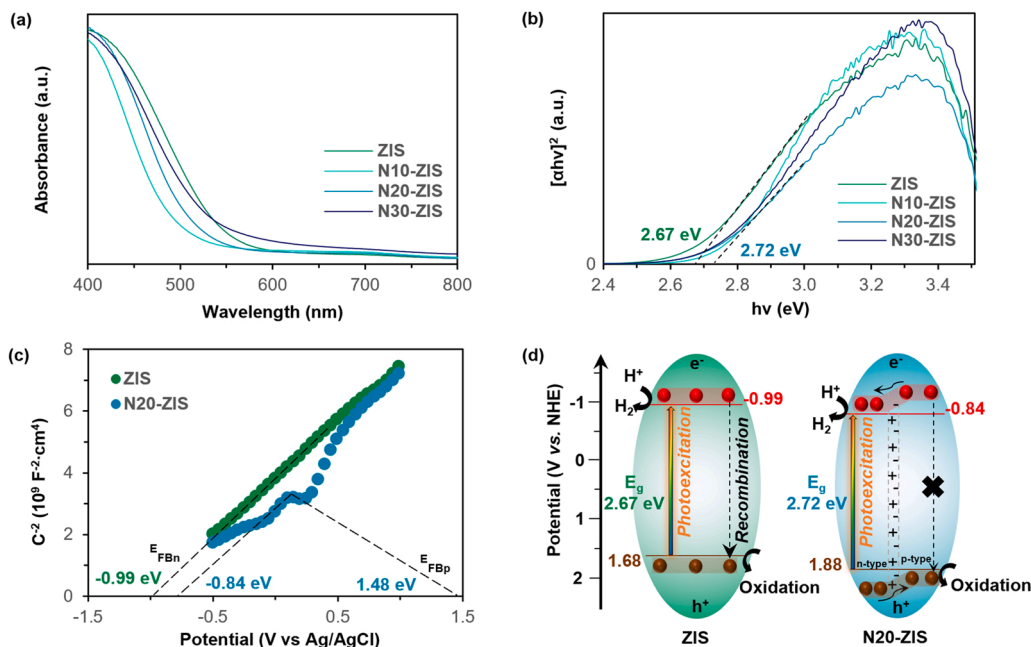


Fig. 5. (a) UV-Vis absorbance spectra and (b) Tauc plot derived from KM relationship against incident photon energy of the respective samples. (c) MS plots and (d) schematic of the band structures of the pristine ZIS and N20-ZIS samples along with the corresponding photoinduced activities.

in which q , ϵ , ϵ_0 represent the electronic charge, material dependent dielectric constant and vacuum permittivity, respectively. As evaluated in Fig. S7, the N_d of N20-ZIS ($9.04 \times 10^{21} \text{ cm}^{-3}$) is denser than ZIS ($7.67 \times 10^{21} \text{ cm}^{-3}$), which is attributed to the differential electronegativity (N dopant and S host atom). This induces charge redistribution in the structure and provides more charge carriers (electrons) for the enhancement of photocatalytic reaction [46]. Furthermore, the presence of acceptor density in N20-ZIS framework will stimulate internal electric potential and facilitate the construction of donor-acceptor structure [47]. Hence, the above analyses insinuate the successful creation of dual p-n charge properties within N-ZIS structure. Consequently, such configuration provides more charge carries for the photoreaction, boosts charge transfer across the built-in electric field, and suppresses electron-hole pairs recombination that collectively enhance the photocatalytic HER performance.

The band edge positions are essential to postulate the flow direction of charge carriers and participation in redox reactions. To begin with, the flat band potential (E_{FB}) can be obtained by extrapolating the respective MS slope towards the potential axis, whereby p-type (E_{FBp}) and n-type flat band (E_{FBn}) correspond to the negative and positive gradient, respectively. As revealed by Fig. 5c, the E_{FBn} of ZIS and N20-ZIS are obtained to be -0.99 and -0.84 V (vs. Ag/AgCl). Additionally, N20-ZIS possesses an E_{FBp} of $+1.48$ V (vs. Ag/AgCl). Following the widely accepted rule of thumb, the conduction band edge (E_{CB}) can be estimated to be -0.2 V than the E_{FBn} while valence band edge (E_{VB}) is 0.2 V more positive than E_{FBp} [13]. Thus, E_{CB} of ZIS and N20-ZIS are calculated to be -1.19 and -1.04 V (vs. Ag/AgCl), while E_{VB} of N20-ZIS is found to be $+1.68$ V (vs. Ag/AgCl). For standardization based on energy conversion, normal hydrogen electrode potential (E_{NHE}) at 0 pH is evaluated following Eq. (5) [48].

$$E_{NHE} = E_{Ag/AgCl} + 0.1967 \quad (5)$$

where $E_{Ag/AgCl}$ is the potential vs. Ag/AgCl. In this regard, the E_{CB} of ZIS and N20-ZIS as well as E_{VB} of N20-ZIS are converted to be -0.99 , -0.84 and $+1.88$ V (vs. NHE), respectively. The unidentified E_{VB} of ZIS can be easily determined to be $+1.68$ V (vs. NHE) via Eq. (6) and the E_g obtained from KM functions.

$$E_{VB} = E_g + E_{CB} \quad (6)$$

It is worth noting that the E_{VB} of N20-ZIS calculated utilizing Eq. (6) exactly matches that of $+1.88$ V (vs. NHE), which was previously determined from MS plot, demonstrating that the result is highly reliant and accurate. The schematic of the band structures for ZIS and N20-ZIS are illustrated in Fig. 5d. In brief, the visible-light active with dual p-n charge properties underlying in the defect-free N20-ZIS framework increases photogeneration of charge carries, enriches charge separation, inhibits electron-hole pairs recombination, and ameliorates charge transfer to active site for desired HER.

For acquisition of deeper understanding on the benefits brought by N-doping, time-resolved photoluminescence (TRPL) measurement was performed as shown in Fig. 6a. All the decay curves follow a bi-exponential kinetic function fitting model as shown in Eq. (7), and the average lifetime (τ_{ave}) of the samples are calculated by Eq. (8) [49].

$$I = A_1 e^{-\frac{t}{\tau_1}} + A_2 e^{-\frac{t}{\tau_2}} \quad (7)$$

$$\tau_{ave} = \frac{A_1 \tau_1^2 + A_2 \tau_2^2}{A_1 \tau_1 + A_2 \tau_2} \quad (8)$$

The model consists of two exponential terms: (1) τ_1 and A_1 represent the short fluorescent lifetime and its relative amplitude, while (2) τ_2 and A_2 denote the long fluorescent lifetime and its relative amplitude. The detailed kinetic fitting parameters are shown in Fig. S9. All the fittings have close-to-unity coefficient of determination (R^2) implying high goodness-of-fit for the model. Summarized in Fig. 6a, TRPL curves of pristine ZIS located at the topmost region accompanied by the longest τ_{ave} of 6.91 ns. Oppositely, the τ_{ave} of N20-ZIS is significantly reduced by ca. 39 % to as low as 4.26 ns, indicating elevated charge migration behavior and promoted electron transfer separating the emissive state across the internal electric field [50]. Additionally, steady-state PL of N20-ZIS is remarkably quenched as compared to the pristine counterpart (see Fig. S10), which collaborates the improvement in elevating charge separation. The shortening of TRPL lifetime and quenching of PL collectively favor charge transfer and suppress electron-hole pairs recombination, imputed to the existence of p-n charge properties within

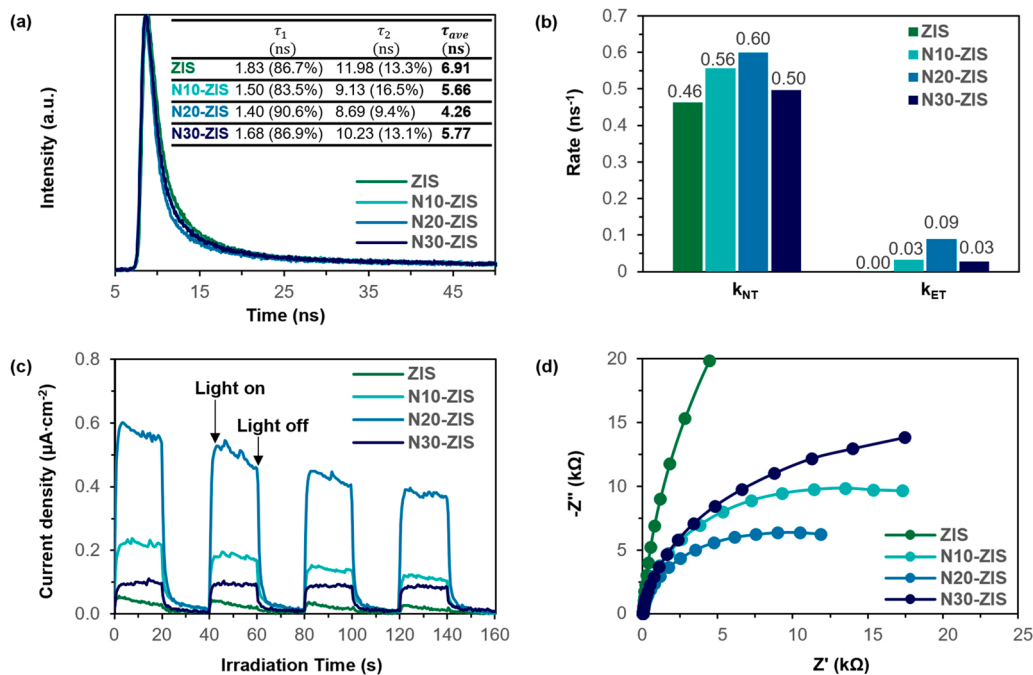


Fig. 6. (a) TRPL spectra with inset showing the model parameters, (b) electron transfer rate constants of k_{NT} and k_{ET} , (c) transient photocurrent responses, and (d) EIS Nyquist plots of the as-synthesized samples.

the N20-ZIS framework which excavates an additional electron transfer pathway in a non-radiative quenching mode [51]. Besides, non-radiative transmission rate (k_{NT}) and electron transfer rate (k_{ET}) can be evaluated via Eqs. (9) and (10) by utilizing the TRPL model kinetic parameters, i.e., τ_1 , τ_2 , $\tau_{ave,ZIS}$ (τ_{ave} for ZIS) and $\tau_{ave,N-ZIS}$ (τ_{ave} of the N-ZIS structures).

$$k_{NT} = \frac{1}{\tau_1} - \frac{1}{\tau_2} \quad (9)$$

$$k_{ET} = \frac{1}{\tau_{ave,N-ZIS}} - \frac{1}{\tau_{ave,ZIS}} \quad (10)$$

As shown in Fig. 6b, N20-ZIS acquires the highest k_{NT} (0.60 ns^{-1}) and k_{ET} (0.09 ns^{-1}), delineating the augmented charge transfer kinetics in the N20-ZIS arising from the existence of p-n induced internal electric field. For complete evaluation of the charge transfer dynamics, transient photocurrent and electrochemical impedance spectroscopy (EIS) Nyquist analysis were conducted. Fig. 6c shows the photocurrent intensity measured in the order of N20-ZIS > N10-ZIS > N30-ZIS > ZIS, which resembles the trend of photocatalytic HER performance (Fig. 4). The photocurrent density is generally expected to be in accordance with the charge separation efficacy and serves as a direct indicator of photocatalytic performance [52]. Thus, the striking photocatalytic improvement of N20-ZIS is undoubtedly contributed by the accelerated photo-induced carriers separation and transfer rate. EIS Nyquist plot depicted in Fig. 6d is used to consolidate the finding of charge migration proficiency. The Nyquist arc radius is in parallel relationship with charge transfer resistance (R_{CT}), details smaller semicircle radius dictates the lower impedance in charge migration [53]. Predictably, the R_{CT} of pristine ZIS is the highest as shown by the drastically larger arc radius indicating deprived charge transfer. On the other hand, N20-ZIS reveals the lowest R_{CT} (smaller arc radii) facilitating transfer of interfacial electron transfers to participate in surface redox reaction. In whole, all the analyses converge to the fact that N-dopant boosted charge transfer behavior of ZIS. The introduction of dual p-n charge nature further promotes the charge dynamics and inhibits the electron-hole pairs recombination. Owing to the correlation observed between photocatalytic HER performance with charge carrier kinetics, it can be established that N-doping induced charge transfer plays a major role in ameliorating photoactivity.

3.4. Insights from theoretical calculations

First-principle density functional theory (DFT) computation was conducted to divulge the effect of N-doping into ZIS structure from the theoretical perspective. Following the construction of 2×2 pristine bilayer ZIS model with 56 atoms as shown in Fig. S11, substitution of intrinsic S by extrinsic N atom was performed. Different substitutional sites (Top layer: S1', S2', S3', S4'; Bottom layer: S1, S2, S3, S4) were studied to establish the potential doping region, where the most stable structure is represented by the lowest formation energy (E_{form}) which is computed following Eq. (11).

$$E_{form} = (E_{N_nZIS} + n\mu_S) - (E_{ZIS} + n\mu_N) \quad (11)$$

in which E_{N_n} is the total energy of N-doped ZIS (with different n number of N atoms), E_{ZIS} is the total energy of pristine ZIS, while μ_S and μ_N are the chemical potentials of the host S atom and N dopant derived from the bulk phase, respectively. Beginning with introduction of one N atom to replace the host S atom, different 1 N-doped ZIS configurations (underdoped) were obtained as shown in Fig. S12. It is clearly seen that only $N_{(4)}$ ZIS structure, substitution of S located at the bottom S4 layer, returns no significant lattice distortion and with the lowest E_{form} of -2.51 eV . This configuration is considered as the most favorable and stable 1 N-doped structure. Subsequently, the degree of doping was investigated to replicate a close-to experimental (optimal- and over-doped) scenario by incessantly introducing extra N into the system.

2 N-doped ZIS (optimal-doped) structure was then modelled as shown in Fig. S13. Interestingly, continuous substitution of bottom S4 layer does not give the most favorable structure (relatively large E_{form} of -3.56 eV), but substitution of top S4' layer forming $N_{(4)(4')}$ ZIS does (lowest E_{form} of -4.25 eV). Owing to the pre-existence of N atom in $N_{(4)}$ ZIS structure reallocating the charge distribution, progressive substitution of N into S4' layer does not cause lattice distortion which had been observed in direct 1 N substitution into S4' forming $N_{(4')}$ ZIS. The doping process was then repeated to form over-doped model with 3 N-ZIS structures as presented in Fig. S14. Despite the most favorable 3 N-ZIS model of $N_{(4)(4')(3)}$ ZIS (lowest E_{form} of -5.61 eV), major structure deformation is observed. Such finding is consistent with experimental where excessive introduction of N into ZIS framework will result in lattice distortion. Figs. 7a – e provide the graphical summary of the theoretical structure modelling. The $N_{(4)(4')}$ ZIS structure is regarded as the simulated model of N20-ZIS due to the close-to-experimental N doping percentage of ca. 3.6 N % (2 N in 56 atoms) and being the most stable structure without lattice distortion. To elucidate the effect of N-doping towards hydrogen evolution reaction, H adsorption free energy (ΔG_{H^*}) was calculated in Eq. (12).

$$\Delta G_{H^*} = \Delta E_{H^*} + (\Delta ZPE - T\Delta S)_{H^*} \quad (12)$$

where ΔE_{H^*} is the differential binding energy of H around favorable active site, ΔZPE is the zero-point energy correction and $T\Delta S$ is the entropy contribution at temperature T. Referring to Sabatier principle, a perfect HER photocatalyst is capable in forming strong bond with adsorbed H^* for facile photoelectron transfer, and simultaneously interacting weakly with reacted molecules for ease of H_2 release [54]. A close-to-zero ΔG_{H^*} then serves as an indicator for good HER photocatalyst as it implies that both the reaction barriers in the adsorption and desorption steps are compromised [55]. Based on the free energy diagram of HER displayed in Fig. 7f and Fig. S15, the ΔG_{H^*} of $N_{(4)(4')}$ ZIS is relatively nearer to zero (-1.49 eV) as compared to pristine ZIS (1.80 eV), indicating the diminishment of adsorption-desorption barriers on the active site for better HER. The result affirms the positive effect of substituting host S by N dopant which induces charge redistribution within the framework for favorable HER kinetics.

To further investigate the alteration of electronic properties and charge behaviors induced by N-dopant, calculations were performed to compute the density of state (DOS) as well as partial DOS (PDOS). As shown in Fig. 8a, the VB of ZIS contains hybridized S 3p and Zn 3d orbitals, whereas CB consists of S 3p and In 5 s orbitals, which is consistent with other reports [56]. Directing attention to Fig. 8b, optimal incorporation of N dopant into ZIS structure introduces deep-level acceptor state down the Fermi level. Consequently, the Fermi level of $N_{(4)(4')}$ ZIS shifts down towards VB region, endowing a p-type behavior [38,57]. Furthermore, the electron density around valence band maximum (VBM) tremendously increases after N-doping which reflects a greater portion of ground state electrons is readily available to be photoexcited to CB for participation of HER. The relative band edge positions of CB and VB were computed through Mulliken electronegativity principle according to Eqs. (6) and (13) [24].

$$E_{CB} = \chi - E_c - 0.5E_g \quad (13)$$

where χ is the absolute electronegativity of the structure and E_c is the energy of free electron. With the details provided in Table S3, N-doping indeed fundamentally leads to downshift of both band edge positions and slight increase of E_g , which is in line with the experimental MS and UV-Vis analysis. Besides band edge positions, more information could be extracted from the calculated PDOS, where band center is one of them. To explore the insights on the non-metal S active sites, S 3p band center (ϵ_p) is computed according to Eq. (14) [58].

$$\epsilon_p = \frac{\int_{-\infty}^{\infty} E \cdot D_{S3p}(E) dE}{\int_{-\infty}^{\infty} D_{S3p}(E) dE} - E_f \quad (14)$$

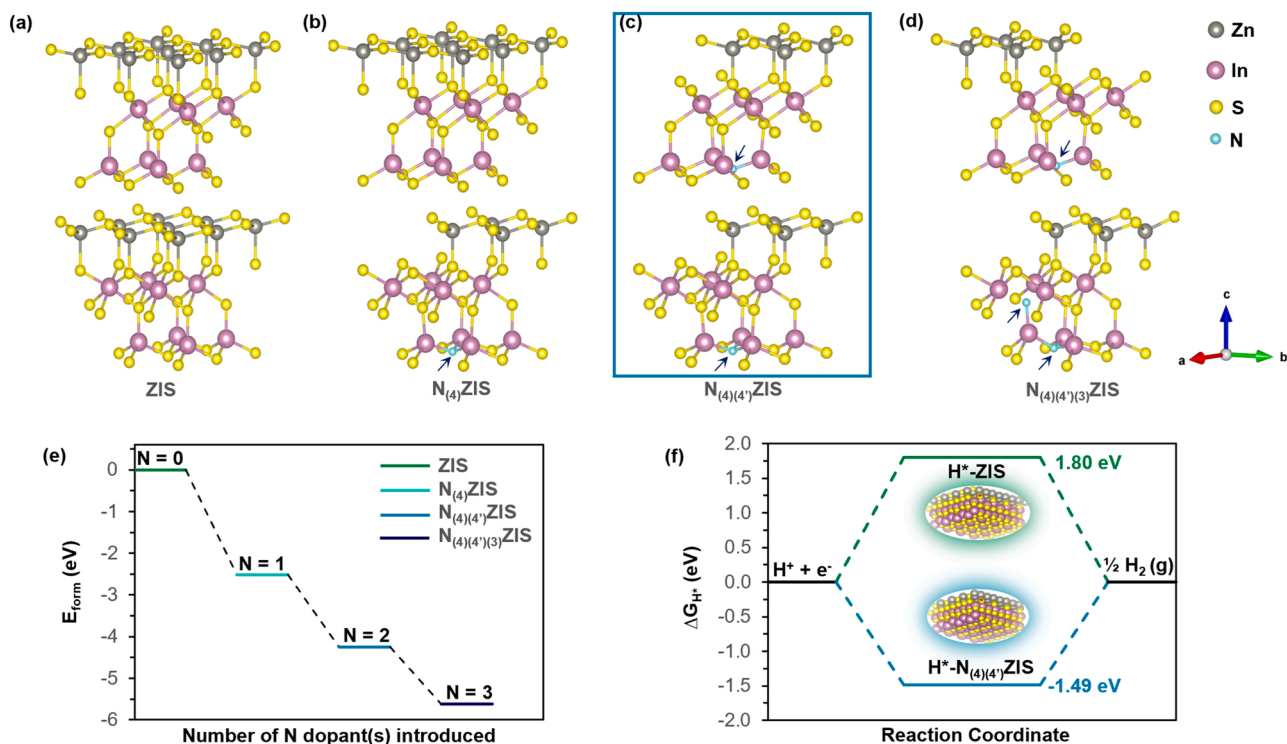


Fig. 7. Optimized structures for (a) pristine ZIS, (b) 1 N-doped ZIS of $N_{(4)}ZIS$, (c) 2 N-doped ZIS of $N_{(4)(4')}ZIS$, and (d) 3 N-doped ZIS of $N_{(4)(4')(3)}ZIS$, with blue arrow directing the presence of N atoms. (e) Graph of E_{form} against different number of N dopant(s) introduced into the ZIS framework. (f) HER free energy diagram for pristine ZIS and $N_{(4)(4')}ZIS$.

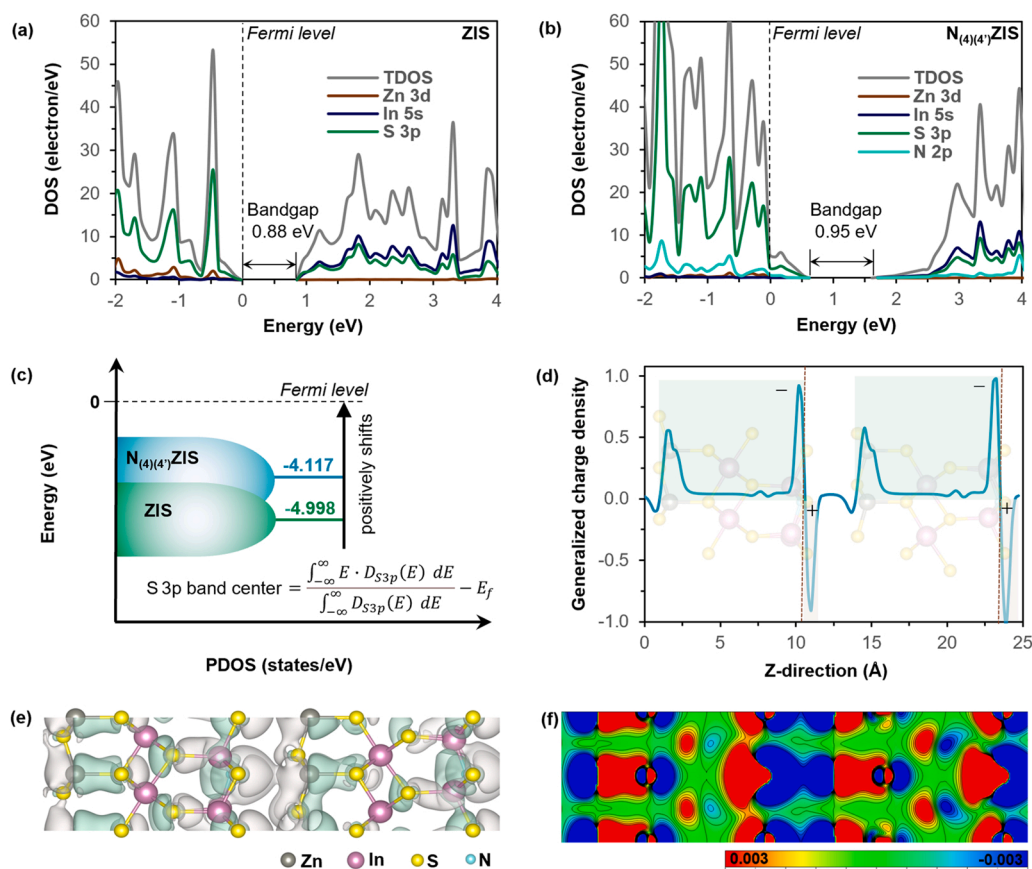


Fig. 8. Calculated DOS for (a) pristine ZIS and (b) $N_{(4)(4')}ZIS$ structures. Fermi level is set to 0 eV. (c) Schematic PDOS plot demonstrating the S 3p band centers of ZIS and $N_{(4)(4')}ZIS$ relative to Fermi level. (d) generalized electron density difference perpendicular to XY plane, (e) calculated 3D charge density difference for $N_{(4)(4')}ZIS$ with green and gray colors represent positive and negative electron density isosurface, respectively, and (f) 2D charge difference cut plane along (110) for $N_{(4)(4')}ZIS$ model.

wherein $D_{S3p}(E)$ represents the energy-dependent DOS projected on the p orbitals of the S element and E_f denotes the Fermi energy of the system (naturally set to 0 eV). According to p-band theory, the surface activity is governed by ϵ_p in which the closer the position of ϵ_p relative to E_f , the greater the electron accumulation and thus the better the surface species adsorption behavior [59]. As reflected in Fig. 8c, the ϵ_p of N-doped ZIS (−4.117 eV) upshifts closer to the E_f compared to pristine ZIS (−4.998 eV). The positive shift of ϵ_p implies higher charge accumulation around active S sites which strongly interact with H^+ to promote photoelectron transfer for HER. This finding coincides not only with the theoretically lower ΔG_{H^+} in $N_{(4)(4')}$ ZIS (favoring adsorption) to reduce HER kinetic barriers, but also the experimental finding with more negative zeta potential of N20-ZIS possessing higher superficial charges to enhance H^+ adsorption. To the point, ϵ_p could serve as an effective signifier for surface H^+ adsorption behavior in concordance to other reports [60,61]. The changes of charge distribution of N-doped ZIS had been studied as depicted in Fig. 8e, where the green region means electron accumulation and gray area shows electron depletion. The 3D charge distribution and the 2D cut plane (Fig. 8f) clearly demonstrates high charge redistribution across the whole framework after introducing extrinsic N with different electronegativity into the structure. Furthermore, the Z-directional planar-averaged charge density difference in Fig. 8d evidently illustrates interfacial charge transfer around the N and surrounding S atoms. The sizeable variation between the positively and negatively charged layers renders formation of dual p-n charge properties and construction of internal electric field as observed in the experiment [62,63]. Concisely, the theoretical calculations align well with the experimental findings and magnificently provide fundamental insights on the advantageous improvement of N-doping towards ZIS, which include (1) dual p-n charge nature improving charge transfer rate, (2) VBM electron density augmentation providing more ground state electrons for photoexcitation, (3) ϵ_p positively translation nearer to E_f indicating higher surface H^+ adsorption, and (4) closer-to-zero ΔG_{H^+} reducing adsorption-desorption barrier for favorable HER.

4. Conclusion

In summary, optimal N-doped ZIS photocatalyst incorporating dual p-n charge properties within the framework has been successfully synthesized via facile one-pot *in-situ* solvothermal route. Introduction of electron-deficient nature of N substituting intrinsic S of ZIS induces co-existence of p-n charge properties in the crystal structure. The presence of dual charge nature enormously facilitates the photogenerated charge transfer dynamics across the internal electric field and suppresses electron-hole pairs recombination. Fundamental study and theoretical analysis further unveil the role of N-dopant provoking charge redistribution across the structure and reducing HER reaction barriers. Consequently, N20-ZIS exhibits $1575.71 \mu\text{mol}\cdot\text{g}^{-1}$ of H_2 under 6-hour irradiation of visible light, which is 6.35 times than that of pristine ZIS. Regardless of pristine ZIS showing insignificant AQY of 0.53 % (420 nm), N20-ZIS microsphere still exhibits high AQY of 6.59 % under the same condition. Both experimental and theoretical findings converge on the same conclusion of N-doping enhances photocatalytic performance. The in-depth analysis carried out in this work could also be extended to other photocatalysts to develop an ultimately efficient HER photocatalyst to achieve the goal of net zero carbon emission.

CRedit authorship contribution statement

Wei-Kean Chong: Conceptualization, Methodology, Software, Formal analysis, Investigation, Visualization, Writing – original draft preparation. **Boon-Junn Ng:** Validation, Data curation, Writing – review & editing, Supervision. **Xin-Ying Kong:** Investigation, Writing – review & editing. **Lling-Lling Tan:** Writing – review & editing, Supervision. **Lutfi Kurnianditia Putri:** Writing – review & editing,

Supervision. **Siang-Piao Chai:** Resources, Validation, Writing – review & editing, Supervision, Project administration, Funding acquisition.

Declaration of Competing Interest

The authors declare that they have no known competing financial interests or personal relationships that could have appeared to influence the work reported in this paper.

Data Availability

Data will be made available on request.

Acknowledgement

This research project was funded by the Malaysia Research University Network (MRUN) from the Ministry of Higher Education Malaysia (Grant No. 304/PJKIMIA/656501/K145). This work was also supported by High-Performance Computer (HPC) and the High Impact Research Support Fund (Ref. No. REU00354) from Monash University Malaysia.

Appendix A. Supporting information

Supplementary data associated with this article can be found in the online version at doi:10.1016/j.apcatb.2023.122372.

References

- [1] Q. Wang, K. Domen, Particulate photocatalysts for light-driven water splitting: mechanisms, challenges, and design strategies, *Chem. Rev.* 120 (2020) 919–985.
- [2] V.N. Rao, P. Ravi, M. Sathish, M. Vijayakumar, M. Sakar, M. Karthik, S. Balakumar, K.R. Reddy, N.P. Shetti, T.M. Aminabhavi, M.V. Shankar, Metal chalcogenide-based core/shell photocatalysts for solar hydrogen production: recent advances, properties and technology challenges, *J. Hazard. Mater.* 415 (2021), 125588.
- [3] H. Xiao, P. Liu, W. Wang, R. Ran, W. Zhou, Z. Shao, Enhancing the photocatalytic activity of ruddlesden-popper Sr_2TiO_4 for hydrogen evolution through synergistic silver doping and moderate reducing pretreatment, *Mater. Today Energy* 23 (2022), 100899.
- [4] X. Han, P. Liu, R. Ran, W. Wang, W. Zhou, Z. Shao, Non-metal fluorine doping in Ruddlesden–Popper perovskite oxide enables high-efficiency photocatalytic water splitting for hydrogen production, *Mater. Today Energy* 23 (2022), 100896.
- [5] Q. Zhu, Z. Xu, Q. Yi, M. Nasir, M. Xing, B. Qiu, J. Zhang, Prolonged electron lifetime in sulfur vacancy-rich ZnCdS nanocages by interstitial phosphorus doping for photocatalytic water reduction, *Mater. Chem. Front.* 4 (2020) 3234–3239.
- [6] M. Choi, H. Choi, J. Ahn, Y.T. Kim, Understanding of relationship between dopant and substitutional site to develop novel phase-change materials based on In_3SbTe_2 , *Jpn. J. Appl. Phys.* 58 (2019) SBBB02.
- [7] W.-K. Chong, B.-J. Ng, L.-L. Tan, S.-P. Chai, Recent advances in nanoscale engineering of ternary metal sulfide-based heterostructures for photocatalytic water splitting applications, *Energy Fuels* 36 (2022) 4250–4267.
- [8] Y. Pan, X. Yuan, L. Jiang, H. Yu, J. Zhang, H. Wang, R. Guan, G. Zeng, Recent advances in synthesis, modification and photocatalytic applications of micro/nano-structured zinc indium sulfide, *Chem. Eng. J.* 354 (2018) 407–431.
- [9] X. Shi, L. Mao, P. Yang, H. Zheng, M. Fujitsuka, J. Zhang, T. Majima, Ultrathin ZnIn_2S_4 nanosheets with active (110) facet exposure and efficient charge separation for cocatalyst free photocatalytic hydrogen evolution, *Appl. Catal., B* 265 (2020), 118616.
- [10] W.-K. Chong, B.-J. Ng, C.-C. Er, L.-L. Tan, S.-P. Chai, Insights from density functional theory calculations on heteroatom P-doped ZnIn_2S_4 bilayer nanosheets with atomic-level charge steering for photocatalytic water splitting, *Sci. Rep.* 12 (2022) 1927.
- [11] B.-J. Ng, L.K. Putri, X.Y. Kong, Y.W. Teh, P. Pasbakhsh, S.-P. Chai, Z-scheme photocatalytic systems for solar water splitting, *Adv. Sci.* 7 (2020) 1903171.
- [12] J. Lee, L.-L. Tan, S.-P. Chai, Heterojunction photocatalysts for artificial nitrogen fixation: fundamentals, latest advances and future perspectives, *Nanoscale* 13 (2021) 7011–7033.
- [13] X. Li, J. Yu, J. Low, Y. Fang, J. Xiao, X. Chen, Engineering heterogeneous semiconductors for solar water splitting, *J. Mater. Chem. A* 3 (2015) 2485–2534.
- [14] M.-Y. Li, Y. Shi, C.-C. Cheng, L.-S. Lu, Y.-C. Lin, H.-L. Tang, M.-L. Tsai, C.-W. Chu, K.-H. Wei, J.-H. He, W.-H. Chang, K. Suenaga, L.-J. Li, Epitaxial growth of a monolayer $\text{WSe}_2\text{-MoS}_2$ lateral p-n junction with an atomically sharp, *Interface, Sci.* 349 (2015) 524–528.
- [15] X. Zhu, N.R. Monahan, Z. Gong, H. Zhu, K.W. Williams, C.A. Nelson, Charge transfer excitons at van der Waals interfaces, *J. Am. Chem. Soc.* 137 (2015) 8313–8320.

- [16] A.A. Puzetky, L. Liang, X. Li, K. Xiao, B.G. Sumpter, V. Meunier, D.B. Geohegan, Twisted MoSe₂ bilayers with variable local stacking and interlayer coupling revealed by low-frequency Raman spectroscopy, *ACS Nano* 10 (2016) 2736–2744.
- [17] H.-M. Li, D. Lee, D. Qu, X. Liu, J. Ryu, A. Seabaugh, W.J. Yoo, Ultimate thin vertical p–n junction composed of two-dimensional layered molybdenum disulfide, *Nat. Commun.* 6 (2015) 6564.
- [18] X. Zhang, Z. Shao, X. Zhang, Y. He, J. Jie, Surface charge transfer doping of low-dimensional nanostructures toward high-performance nanodevices, *Adv. Mater.* 28 (2016) 10409–10442.
- [19] Z. Ai, K. Zhang, D. Shi, B. Chang, Y. Shao, L. Zhang, Y. Wu, X. Hao, Band-Matching Transformation between CdS and BCNTs with tunable p–n homojunction for enhanced photocatalytic pure water splitting, *Nano Energy* 69 (2020), 104408.
- [20] W. Jin, X. Zeng, Z. Guo, Y. Zeng, W. Wang, Y. Zeng, Y. Hu, Y. Xiao, J. Lu, J. Lu, J. Wang, Optoelectronic properties of lateral MoS₂ p–n homojunction implemented by selective p-type doping using nitrogen plasma, *J. Phys. D.* 53 (2020), 405102.
- [21] J.P. Perdew, M. Ernzerhof, K. Burke, Rationale for mixing exact exchange with density functional approximations, *J. Chem. Phys.* 105 (1996) 9982–9985.
- [22] X. Zhou, H. Dong, A.-M. Ren, Exploring the mechanism of water-splitting reaction in NiO_x/β-Ga₂O₃ photocatalysts by first-principles calculations, *Phys. Chem. Chem. Phys.* 18 (2016) 11111–11119.
- [23] S. Grimme, S. Ehrlich, L. Goerigk, Effect of the damping function in dispersion corrected density functional theory, *J. Comput. Chem.* 32 (2011) 1456–1465.
- [24] C.-C. Er, J.-Y. Tang, C.-M. Fung, L.-L. Tan, N.V. Medhekar, S.-P. Chai, Atomistic insights into the reformation of CH₄ with CO₂ on metal-free g-C₃N₄: unraveling the reaction mechanisms using first-principles DFT calculations, *J. Phys. Chem. C* 125 (2021) 23021–23028.
- [25] Z.-T. Hu, W.-H. Xing, S.-Y. Gong, T. Sun, C. Wang, M. Hu, J. Zhao, Z. Pan, W. Chen, Z. Chen, X. Li, Flower-like ZnIn₂S₄ microspheres with highly efficient catalytic activity for visible-light-driven sulfamethoxazole photodegradation, *Colloids Surf. A Physicochem. Eng. Asp.* 643 (2022), 128779.
- [26] X. Wang, X. Wang, J. Huang, S. Li, A. Meng, Z. Li, Interfacial chemical bond and internal electric field modulated Z-scheme S₂-ZnIn₂S₄/MoSe₂ photocatalyst for efficient hydrogen evolution, *Nat. Commun.* 12 (2021) 4112.
- [27] P. Wang, Z. Shen, Y. Xia, H. Wang, L. Zheng, W. Xi, S. Zhan, Atomic insights for optimum and excess doping in photocatalysis: a case study of few-layer Cu-ZnIn₂S₄, *Adv. Funct. Mater.* 29 (2019) 1807013.
- [28] Z. Li, X. Wang, W. Tian, A. Meng, L. Yang, CoNi bimetal cocatalyst modifying a hierarchical ZnIn₂S₄ nanosheet-based microsphere noble-metal-free photocatalyst for efficient visible-light-driven photocatalytic hydrogen production, *ACS Sustain. Chem. Eng.* 7 (2019) 0–20201.
- [29] J.C. Slater, Atomic radii in crystals, *J. Chem. Phys.* 41 (1964) 3199–3204.
- [30] C. Du, B. Yan, Z. Lin, G. Yang, Enhanced carrier separation and increased electron density in 2D heavily N-doped ZnIn₂S₄ for photocatalytic hydrogen production, *J. Mater. Chem. A* 8 (2020) 207–217.
- [31] Y. Zhou, G. Chen, Y. Yu, Y. Peng, Y. Zheng, F. He, Z. Han, An efficient method to enhance the stability of sulphide semiconductor photocatalysts: a case study of N-Doped ZnS, *Phys. Chem. Chem. Phys.* 17 (2015) 1870–1876.
- [32] Y. Li, Z. Jin, T. Zhao, Performance of ZIF-67 – derived fold polyhedrons for enhanced photocatalytic hydrogen evolution, *Chem. Eng. J.* 382 (2020), 123051.
- [33] X. Yan, Z. Jin, Interface engineering: NiAl-LDH *in-situ* derived NiP₂ quantum dots and Cu₃P nanoparticles ingeniously constructed p–n heterojunction for photocatalytic hydrogen evolution, *Chem. Eng. J.* 420 (2021), 127682.
- [34] X. Hao, Y. Shao, D. Xiang, Z. Jin, Amorphous WP-modified hierarchical ZnIn₂S₄ nanoflowers with boosting interfacial charge separation for photocatalytic H₂ evolution, *Adv. Mater. Interfaces* 9 (2022) 2200185.
- [35] M. Qureshi, K. Takanabe, Insights on measuring and reporting heterogeneous photocatalysis: efficiency definitions and setup examples, *Chem. Mater.* 29 (2017) 158–167.
- [36] K. Takanabe, Addressing fundamental experimental aspects of photocatalysis studies, *J. Catal.* 370 (2019) 480–484.
- [37] P. Makula, M. Pacia, W. Macyk, How to correctly determine the band gap energy of modified semiconductor photocatalysts based on UV–Vis spectra, *J. Phys. Chem. Lett.* 9 (2018) 6814–6817.
- [38] Y. Wu, X. Liu, H. Zhang, J. Li, M. Zhou, L. Li, Y. Wang, Atomic sandwiched p–n homojunctions, *Angew. Chem. Int. Ed.* 60 (2021) 3487–3492.
- [39] A. Nipane, D. Karmakar, N. Kaushik, S. Karande, S. Lodha, Few-layer MoS₂ p-type devices enabled by selective doping using low energy phosphorus implantation, *ACS Nano* 10 (2016) 2128–2137.
- [40] M. Chiesa, S. Livraghi, M.C. Paganini, E. Salvadori, E. Giamello, Nitrogen-doped semiconducting oxides. implications on photochemical, photocatalytic and electronic properties derived from EPR spectroscopy, *Chem. Sci.* 11 (2020) 6623–6641.
- [41] L.K. Putri, B.-J. Ng, W.-J. Ong, H.W. Lee, W.S. Chang, S.-P. Chai, Engineering Nanoscale p–n junction via the synergetic dual-doping of p-type boron-doped graphene hybridized with n-type oxygen-doped carbon nitride for enhanced photocatalytic hydrogen evolution, *J. Mater. Chem. A* 6 (2018) 3181–3194.
- [42] N. Sagara, S. Kamimura, T. Tsubota, T. Ohno, Photoelectrochemical CO₂ reduction by a p-type boron-doped g-C₃N₄ electrode under visible light, *Appl. Catal., B* 192 (2016) 193–198.
- [43] K. Dolui, I. Rungger, C. Das Pemmaraju, S. Sanvito, Possible doping strategies for MoS₂ monolayers: an ab initio study, *Phys. Rev. B* 88 (2013), 075420.
- [44] K. Sivula, Mott–Schottky analysis of photoelectrodes: sanity checks are needed, *ACS Energy Lett.* 6 (2021) 2549–2551.
- [45] Y. Zhong, Y. Wu, B. Chang, Z. Ai, K. Zhang, Y. Shao, L. Zhang, X. Hao, A CoP/CdS/WS₂ p–n–n tandem heterostructure: a novel photocatalyst for hydrogen evolution without using sacrificial agents, *J. Mater. Chem. A* 7 (2019) 14638–14645.
- [46] Z. Hu, L. Yuan, Z. Liu, Z. Shen, J.C. Yu, An elemental phosphorus photocatalyst with a record high hydrogen evolution efficiency, *Angew. Chem. Int. Ed.* 55 (2016) 9580–9585.
- [47] S. Yu, B. Huang, Y. Dai, W. Wei, A. New, Concept of atomically thin p–n junction based on Ca₂N/Na₂N donor–acceptor heterostructure: a first-principles study, *Nanoscale* 14 (2022) 9661–9668.
- [48] Y.-H. Chew, B.-J. Ng, X.Y. Kong, L.K. Putri, J.-Y. Tang, L.-L. Tan, S.-P. Chai, Interfacial engineering of a zinc blende/wurtzite homojunction photocatalyst through hybridization with a cobalt phosphide co-catalyst for enhanced visible-light-driven photocatalytic H₂ Evolution, *Sustain. Energy Fuels* 4 (2020) 1822–1827.
- [49] J. Chen, C. Zhang, X. Liu, L. Peng, J. Lin, X. Chen, Carrier dynamic process in all-inorganic halide perovskites explored by photoluminescence spectra, *Photon. Res.* 9 (2021) 151–170.
- [50] E. Mitchell, A. Law, R. Godin, Interfacial charge transfer in carbon nitride heterojunctions monitored by optical methods, *J. Photochem. Photobiol. C* 49 (2021), 100453.
- [51] S. Wang, B.Y. Guan, X.W.D. Lou, Construction of ZnIn₂S₄–In₂O₃ hierarchical tubular heterostructures for efficient CO₂ Photoreduction, *J. Am. Chem. Soc.* 140 (2018) 5037–5040.
- [52] X.Y. Kong, W.L. Tan, B.-J. Ng, S.-P. Chai, A.R. Mohamed, Harnessing Vis–NIR broad spectrum for photocatalytic CO₂ reduction over carbon quantum dots-decorated ultrathin Bi₂WO₆ nanosheets, *Nano Res.* 10 (2017) 1720–1731.
- [53] S.H.W. Kok, J. Lee, L.-L. Tan, W.-J. Ong, S.-P. Chai, MXene—a new paradigm toward artificial nitrogen fixation for sustainable ammonia generation: synthesis, properties, and future outlook, *ACS Mater. Lett.* 4 (2022) 212–245.
- [54] M. Che, Nobel prize in chemistry 1912 to sabatier: organic chemistry or catalysis? *Catal. Today* 218–219 (2013) 162–171.
- [55] K.-W. Park, A.M. Kolpak, Mechanism for spontaneous oxygen and hydrogen evolution reactions on CoO nanoparticles, *J. Mater. Chem. A* 7 (2019) 6708–6719.
- [56] X. Shi, C. Dai, X. Wang, J. Hu, J. Zhang, L. Zheng, L. Mao, H. Zheng, M. Zhu, Protruding Pt single-sites on hexagonal ZnIn₂S₄ to accelerate photocatalytic hydrogen evolution, *Nat. Commun.* 13 (2022) 1287.
- [57] Q. Yue, S. Chang, S. Qin, J. Li, Functionalization of monolayer MoS₂ by substitutional doping: a first-principles study, *Phys. Lett. A* 377 (2013) 1362–1367.
- [58] C.-C. Er, L.K. Putri, B.-J. Ng, J.-Y. Tang, N.V. Medhekar, S.-P. Chai, Allotropes selection apropos of photocatalytic CO₂ reduction from first principles studies, *Mater. Today Phys.* 26 (2022), 100751.
- [59] W. Pei, S. Zhou, Y. Bai, J. Zhao, N-doped graphitic carbon materials hybridized with transition metals (compounds) for hydrogen Evolution reaction: understanding the synergistic effect from atomistic level, *Carbon* 133 (2018) 260–266.
- [60] J. Wang, X. Li, B. Wei, R. Sun, W. Yu, H.Y. Hoh, H. Xu, J. Li, X. Ge, Z. Chen, C. Su, Z. Wang, Activating basal planes of NiPS₃ for hydrogen evolution by nonmetal heteroatom doping, *Adv. Funct. Mater.* 30 (2020) 1908708.
- [61] J. Wang, Z. Zhang, H. Song, B. Zhang, J. Liu, X. Shai, L. Miao, Water dissociation kinetic-oriented design of nickel sulfides via tailored dual sites for efficient alkaline hydrogen evolution, *Adv. Funct. Mater.* 31 (2021) 2008578.
- [62] Y. Wu, S. Yao, G. Lv, Y. Wang, H. Zhang, P. Liao, Y. Wang, Construction of p–n junctions in single-unit-cell ZnIn₂S₄ nanosheet arrays toward promoted photoelectrochemical performance, *J. Catal.* 401 (2021) 262–270.
- [63] E. Zhang, Q. Zhu, J. Huang, J. Liu, G. Tan, C. Sun, T. Li, S. Liu, Y. Li, H. Wang, X. Wan, Z. Wen, F. Fan, J. Zhang, K. Ariga, Visually resolving the direct Z-scheme heterojunction in CdS@ZnIn₂S₄ hollow cubes for photocatalytic evolution of H₂ and H₂O₂ from pure water, *Appl. Catal., B* 293 (2021), 120213.